28 May 2010, 8:00 am - 8:30 am

Recent Advances in Terrestrial Lidar Applications in Geotechnical Earthquake Engineering

Roberto Kayer
U.S. Geological Survey, Menlo Park, CA

Jonathan P. Stewart
University of California, Los Angeles, CA

Brian D. Collins
U.S. Geological Survey, Menlo Park, CA

Fifth International Conference on
Recent Advances in Geotechnical Earthquake Engineering and Soil Dynamics
and Symposium in Honor of Professor I.M. Idriss
May 24-29, 2010 • San Diego, California

RECENT ADVANCES IN TERRESTRIAL LIDAR APPLICATIONS IN GEOTECHNICAL EARTHQUAKE ENGINEERING

ROBERT KAYEN
U.S. Geological Survey
Menlo Park, CA 94025, USA

JONATHAN P. STEWART
University of California, Los Angeles
Los Angeles, CA, 90025 USA

BRIAN D. COLLINS
U.S. Geological Survey
Menlo Park, CA 94025, USA

ABSTRACT

During the past five years, geotechnical earthquake engineering and ground deformation research has benefited from the advent of terrestrial LIDAR technology, a revolutionary tool for characterizing fine-scale changes in topography. For ground deformation research, LIDAR is particularly useful for characterizing the dimensions of failures and for monitoring subtle deformations through time. Tripod mounted LIDAR systems have accuracies of approximately 0.4-2.0 cm, and can illuminate targets up to one kilometer away from the sensor. During several minutes of LIDAR scanning, millions of survey position points are collected and processed into an ultra-high resolution terrain model. During earthquake reconnaissance efforts, the detailed failure morphologies of landslides and liquefaction sites can be measured remotely and in a way that is either impractical or impossible by conventional survey means. The ultra-high resolution imagery of the complex surface morphology of ground failures allows the exploration and visualization of damage on a computer in orientations and scales not previously possible. Detailed understanding of the ground surface morphology allows for better numerical modeling of potential failure modes, deformation patterns, and morphologies. Finally, LIDAR allows for the permanent archiving of 3-D terrain models. In this paper, we present the evaluation of the accuracy, bias and dispersion of LIDAR data under controlled experimental conditions. Field applications of LIDAR-damage visualization and analysis are presented from data gathered during the 2004 Niigata Chuetsu (M6.6) earthquake and the 2007-2008 PARI-Ishikari, Hokkaido blast-liquefaction experiment.

INTRODUCTION

Investigations of extreme earthquake events provide the opportunity to learn important lessons and to advance understanding. The primary role of LIDAR technology in characterization of geotechnical earthquake engineering ground failures is to survey and document key aspects of failures in order to develop well-documented case histories, and to provide the basis for numerical back analysis of the slope instability. LIDAR technology has recently served an important role in earthquake engineering research by advancement of our understanding of the complex geometric aspects of landslides, soil liquefaction, and earth structures. Historically, data describing ground failure geometries were collected using conventional data recording and measurement tools such as photography, note taking, and tape surveying. Advanced laser mapping technologies now offer the opportunity to visualize and dramatically improve both the quality and quantity of data collected during investigations.

FIELD AND DATA PROCESSING OF TERRESTRIAL LIDAR

The terrestrial LIDAR technique (3D laser scanning) consists of sending and receiving laser pulses to build a point file of three-dimensional coordinates of the scanned surface. The time of travel for a single pulse reflection is measured along a known trajectory such that the distance from the laser, and consequently the position of a point of interest, is computed. Using this methodology, data collection occurs at rates of thousands of points per second generating a "point cloud" of three-dimensional coordinates.

The USGS Western Coastal and Marine Geology program utilizes two Riegl laser scanners as tripod mounted survey instruments. Multiple scans are collected during each survey to fill in "shadow zones" of locations not directly in the line of sight of the laser and to expand the range and density of the point data. Traditional set up is on a tripod, which is complicated by the low elevation of the scanner and long

shadows cast by objects. In order to see above vegetation and minimize shadow zones, the USGS has developed a pneumatic mast-pole system for elevating the laser 20 meters above the ground (Figure 1 B & C). This system has greatly improved the range and effectiveness of data collection. Laser data are collected at rates of 8000-12,000 points per second, scanning 360 degrees in the horizontal direction and plus and minus 40 degrees from the horizontal in the vertical direction. Georeferenced coordinates of the scan locations are determined by either locating the instrument over known survey benchmarks, collecting GPS data via an antenna mounted directly to the laser, or total station targeting. Acquisition and processing of the data are performed using Riegl and I-SiTE software (I-SiTE, 2007) specifically designed to handle laser scan data..

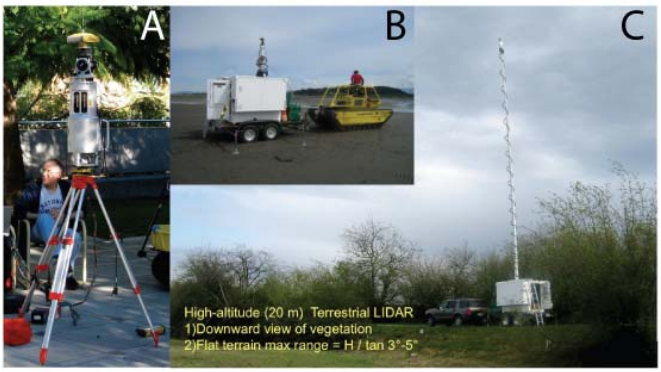

Figure 1. Terrestrial LIDAR scanning is traditionallly performed on a 2 meter tripod (A). The USGS telescopic mast-pole vehicle 'Space Needle' elevates the laser 20 meters above the ground to minimize shadow zones.

Data points in scans are collected at a low point density (<1.0 million points each) to ultrahigh point density (20-60 million points each) depending on the need of the project. When collecting RTK-GPS data, survey control for each scan is typically obtained by utilizing a pair of continuously operating geodetic-quality, dual-frequency (L1/L2) GPS receivers. One receiver was mounted to the scanner while the second acts as a fixed, temporary base station located within 1 km of each scanner position. The fixed base station was set up directly over a known benchmark, and the antenna height above the benchmark was measured to the nearest millimeter. Data collected by the "roving" receiver attached to the scanner is differentially corrected against the antenna height corrected base station position transmitted in real time. Rover receiver RMSE accuracy is ideally maintained at centimeter levels in both horizontal and vertical directions.

Point data from each set of scans are subjected to a series of filters to remove non-ground surface and extraneous laser returns from the point clouds (Figure 2). Points reflected from vegetation, power lines, and other non-ground or water conveyance features were manually cropped from each of the point clouds. Next, an isolated point filter was used to remove single point instances occurring above or below the land surface. These isolated points are usually a result of reflections from moisture in the atmosphere, or reflections off standing water. Topographic filters that select the lowest point in the point clouds were used to remove vegetation from point clouds. Here, the entire data set was divided into 2 to 10 cm square bins, and only the lowest point within the bin selected. Where the LIDAR point cloud partially penetrates through vegetation and reflects from the ground, this filter eliminates most vegetation data points

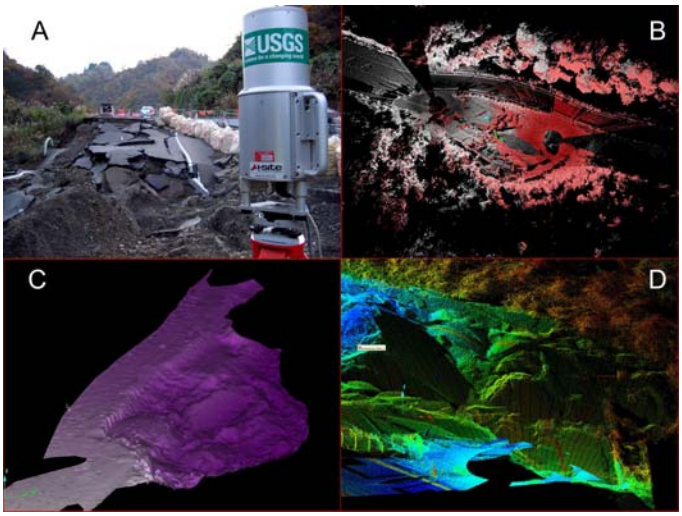

Figure 2. Processing procedures for ground-LIDAR technology: (A) scan target; (B) merge multiple scans; (C) render the solid surface model; (D) visualize by overlying the color on top of the rendered surface and analyze deformations. The direction arrows are the local orientation of the scanner and not the absolute orientation.

In some scans, the vast majority of the point data collected represented vegetation and not the ground surface (densely-vegetated ground). In this case, the topographic filter selects the lowest vegetation point that is different and higher and in elevation than the ground surface. This is the primary manner by which vegetation creates errors in a bare earth model. Finally, for generating topographic surfaces of the ground failure areas, a 2-10 cm minimum separation filter was applied to construct a data set with a less dense network of points. This provides a point data set that enables rapid surface rendering. We use a common reference system (WGS84), and a common vertical datum (NGVD 1988) for LIDAR and total station measurements. The bulk of LIDAR data processing occurs when the individual scan data sets are merged to form a single model of the area of interest, termed the registration process. Georeferencing is performed when the scans are assigned geographic coordinates consistent with a pre-selected datum and projection. If the geographic locations of one or more of the scan origins are known, these steps can be performed concurrently. When a total station survey data is used, several scan tripod set ups are located directly above the known points, and all other scans were registered relative to these fixed scans. In the scanning efforts where RTK GPS

data is collected, geographic coordinates for all scanner locations are known directly. All scans are registered by rotating each additional scan about its origin to obtain a best fit of the data to neighboring scans. Because the origin of each scan position was known and considered fixed, translation of scans was not allowed, thus constraining three of the six degrees of freedom for a single point location. By utilizing three independent scan locations arranged in a near-equilateral triangle, the other three degrees of freedom are constrained by the best fit rotation of each scan to its neighbor in the triangle.

The best fit rotation registration process uses a surface registration algorithm to align the overlapping data within a pair of scans. The algorithm best fit is improved by using "rough" topography (defined as jagged, non-flat edges and objects), which is generally provided by using all available ground data points for a site. However, data associated with vegetation and transient objects (wires, cars, people, moving structures) were removed as they do not provide consistent features for matching between neighboring scans. Registration error using this method is 4 cm under the best conditions. To improve the registration fit, each scan is modeled as a surface and the registration algorithm is recalculated using the best fit between each scan and the surface triangulation of its neighboring scan. Because the point density of a continuous surface is infinite, this resulted in a decrease of the average registration error. At the time of this writing, the best method for registration appears to be reflector-based. Instead of finding the best fit to millions of point cloud values, this algorithm finds the best fit among a small number (< dozen) of reflectors or prisms carefully positioned in the field, and the known scanner positions. Registration error using this method can fall below 2 cm.

The final product of LIDAR data processing is the generation of three-dimensional surface models. A linear interpolation method is used in the processing of surface models: linear interpolation is used to generate surface edges of TIN facets between points. Triangular irregular network (TIN) models represent a topographic surface of each area. After filtering (see above), a TIN surface was generated from each scan file using either a spherical surface algorithm (curved facets) or a linear topographic algorithm (flat facets) (I-SiTE, 2007). Because spherical triangles typically model near-vertical to vertical point data better than linear triangles, this algorithm is better suited for the steep topography of ground failures when compared to typical topographic triangulation algorithms.

GEOSTATISTICS ON POINT CLOUD ACCURACY AND DISPERSION

At a controlled field test site at the Los Angeles Reservoir, operated by the City of Los Angeles Department of Water and Power (LADWP), we evaluated the elevation accuracy of terrestrial LIDAR in the fall of 2007 by comparing measurements made before and after trenching a flat field, against carefully benchmarked total station measurements. The pre-trench conditions were evaluated based on four terrestrial LIDAR scans, performed alongside measurements made with Trimble GX 3D Scanner and Trimble Total Station devices. The trench was excavated on the same day. Three post-trench terrestrial scans were taken along with conventional total station surveys using the same equipment as for pre-trench surveys (Stewart et al, 2009; Kayen et al. 2008, Kayen et al. 2009). In the Stewart et al. 2009 investigation, a corresponding analysis of airborne LIDAR measurements were also made, but are not presented here.

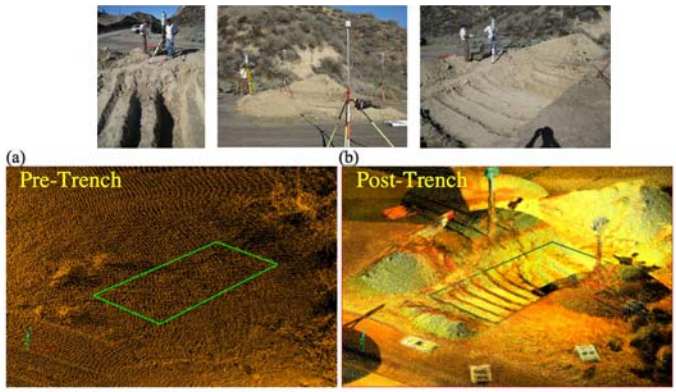

Point clouds from terrestrial lidar showing isometric view of site in a) pre-trench condition and b) post-trench condition. For scale, the outline of the trench shown is approximately 3m by 6m.

Figure 3. Point clouds from terrestrial LIDAR showing isometric view of site in a) pre-trench condition and b) post-trench condition. For scale, the outline of the trench shown is approximately 3m by 6m.

Figure 3 shows terrestrial LIDAR scans of the trench area before and after trenching. The trench site's bare-earth condition is nearly ideal for LIDAR measurement of the ground surface. Elevation residuals for the pre-trench and post-trench conditions were evaluated as described above, except that the LIDAR elevation is taken without interpolation and the total station survey elevation is linearly interpolated due to the very high point density achieved with the Trimble scanner system. Histograms and their statistics are given in Figure 4. The terrestrial LIDAR elevations have very small bias (1-2 cm). Standard deviations for the relatively flat ground, pre-trench conditions are approximately 4-6 cm, which are slightly below those observed in previous studies for similarly ideal conditions. The standard deviations for post-trench conditions are larger than those for pre-trench and are likely associated with horizontal position errors between the LIDAR and total station measurements over the complex topography of the trench.

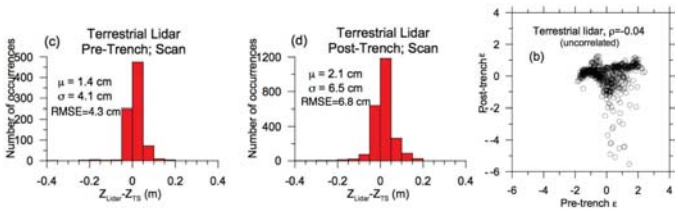

Figure 4. Bias and dispersion of Pre- and Post-Trench terrestrial LIDAR measurements, and correlogram of the pre- and post-trench residuals (after Stewart et al., 2009).

From a comparison of pre- and post-trench elevations, correlations of multi-epoch elevation residuals and statistics can be made. Every pre-trench point with a measured elevation (by conventional surveying or LIDAR) is associated with the laterally closest post-trench point established by the same measurement method. Normalized residuals are calculated for point i in one of the epochs as:

$$\varepsilon_i = \frac{R_i - \mu}{\sigma} \quad (1)$$

where εi = normalized residual for point i, Ri = residual for point i (difference of elevations), and μ and σ are the measurement bias and dispersion. Normalized residuals calculated in this manner for pre- and post-trench epochs are plotted against each other in Figure 4 for data sets derived from airborne and terrestrial LIDAR. Correlation coefficients are calculated as:

$$\rho = \frac{\sum_i \left[(\varepsilon_i)_{pre} \times (\varepsilon_i)_{post} \right]}{\sqrt{\sum_i (\varepsilon_i)^2_{pre} \times \sum_i (\varepsilon_i)^2_{post}}} \quad (2)$$

where subscripts 'pre' and 'post' refer to pre-trench and post-trench epochs, respectively. As shown in Figure 5, the terrestrial LIDAR residuals from the two epochs are nearly uncorrelated. This suggests that the error sources are either stochastic or significantly different for the two epochs. One significant difference between epochs is the post-trench sloping ground condition. We believe this causes the relatively large post-trench values of ε for terrestrial LIDAR data. The lack of coincident pre- and post-trench positions of elevation points contributes to the scatter of the data in Figure 5.

LIQUEFACTION-RELATED GROUND DEFORMATIONS, ISHIKARI JAPAN

Liquefaction ground failure during earthquakes can often result in subtle ground deformations barely perceptable at the decimeter level. In October 2007, the Port and Airport Research Institute (PARI) of the Japan Ministry of Land, Infrastructure and Transportation conducted a large-scale blast-induced liquefaction experiment in Ishikari, Hokkaido, Japan to assess the performance of paved ground subjected to liquefaction. At the site, 5-7 m of loose silty sand was placed as hydraulic fill on natural alluvial sand as an expansion of the Ishikari port facility. Approximately 24,000 m2 of the loose silty sand ground was liquefied using controlled blasting techniques to investigate the performance of airport infrastructure. On a portion of the liquefied site, three 20 m by 50 m test sections were constructed to investigate the performance of improved ground beneath asphalt runways, concrete runway aprons, and open areas. The three ground improvement techniques investigated were sand-cement mixing, vertical drains, and colloidal silica injection. To image the tarmac surface, the scanner is mounted on an elevated platform adjacent to the test site used to elevate the scanner 20 meters above the ground for collection of some of the imagery. Otherwise, a tripod was used on the ground, the embankment, or the electronics box that was part of the experiment.

An oblique image of the study area immediately after the blast experiment can be seen in Figure 5 with the lower corner (to the left of the words "scan point") of the tarmac settled and flooded with liquefied soil. In order to produce elevation difference maps of the tarmac (tp) measure settlements, surface models were produced from the pre-blast and post-blast data sets. The pre-scan LIDAR data was used as a control on the experiment to measure the ground settlement. A series of standard processing steps is followed to produce a surface model; (1), the individual scans were merged together by assigning one scan as the fixed registered reference, with scanner origins of x=0,y=0,z=0, and then referencing the other scans to it using a least-squares "best-fit" match between scan points or reflectors; and (2) to adjust the data to global coordinate system WGS84, reflector targets and scanner positions in the merged data set were precisely surveyed with a differential global positioning system (DGPS). Transformation of the scans to each other and to global coordinates requires data translation and rotation. Once the data are filtered, as previously discussed, surface models can be rendered. Multiple processed surfaces are used to measure change of volumes, areas, and distances

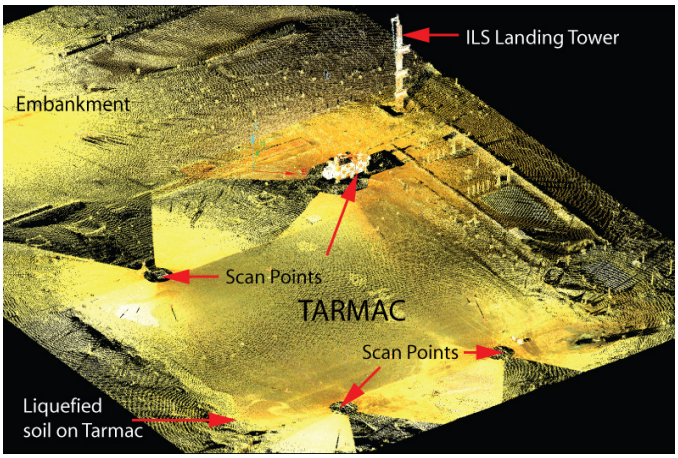

Figure 5. An oblique image of the PARI test site with the circular no-data area below the laser scan location.

Topographic changes in Figure 6 are a map of the difference in elevation between the pre-blast surveys and surveys taken the day of the experiment. In the map, there are three distinct zones of settlement on the PARI tarmac test site. The left (southwest) portion of the test site sits on unimproved ground and this area suffered maximum settlements of between 0.25m and 0.40m. The scale on the right in Figure 6 is a probability distribution function (PDF) for settlements. A peak in the range of 0.25-0.40 m is associated with the unimproved zone. The deformations in the unimproved zone area are not

significantly effected by the perimeter of the tarmac as can be seen in the random contours at the margins of this area. The central zone and the right zone (northeast) are improved ground experiments using compaction grouting and chemical grout injection with different depth of improvement. Both zones had maximum benefit from the grouting in the center of the improved areas, and both ground improvement strategies in these sections did well to minimize settlements. A bridging and flexing of the tarmac about the center of each ground improvement zone was observed within both areas. This zone overlies a swath of unimproved ground separating the improved zones.

In the central portion of each improved zone, the ground appears to have not settled at all. The grouted zone in the PDF is associated with the peak centered about 0.0m and extending from +0.0 m to -0.08m. Settlements at the perimeter of the improved areas may indicate that these areas, closer to the actual blast charges may indicate the soil beneath the center of the improved zone did not liquefy. The settlements near the margins of the improved zone may better reflect the likely settlements during an actual earthquake. The valley of settlement between the two improved ground zones probably reflects a bridging of the tarmac over the unimproved zone. In the PDF, the peak associated with this topographic valley ranges from -0.12 to -0.18m. In the absence of the grouted zones adjacent to the valley, and the bridged tarmac, this zone should have settled more. It is possible be that voids developed beneath this zone of bridged pavement between the two improved zones. Subsequent measurements made at the site 2 days, 4 days, and 5 months after the liquefaction event indicated that no additional settlements occurred at the tarmac site.

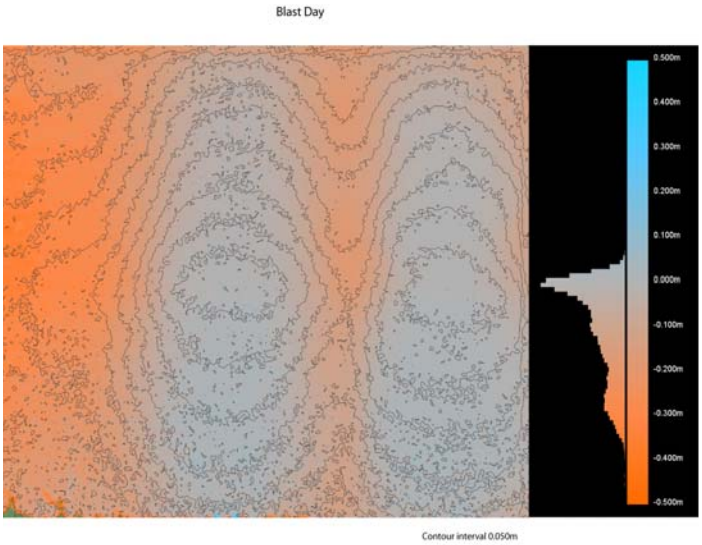

Figure 6. Topographic elevation change difference map showing settlement of the test area on the day of the blast experiment. Maximum settlements are in red.

LIDAR EXAMPLES FROM THE 2004 NIIGATA CHUETSU M7.1 EARTHQUAKE

The Mw 6.6 earthquake that struck Niigata Prefecture on the evening of October 23, 2004, was the most significant earthquake to affect Japan since the 1995 Kobe earthquake. Forty people were killed, almost 3,000 were injured, and hundreds of large landslides destroyed entire upland villages. Total damages are estimated by Japanese authorities at US$40 billion, making this the second most costly disaster in history, after the 1995 Kobe earthquake. The epicenter was in northwestern Honshu, about 80 km south of Niigata City (population 500,000) beneath the Uonuma Hills east of the Shinano River.

Landslides that occurred during the earthquake were of many types: earthflows, debris slides, debris flows, earth slumps and lateral spreads. The landslides also had a variety of effects: some dammed streams, creating new lakes likely to overtop their new embankments at any moment and cause flash floods and mudslides; others buried houses and roads; and some permanent ground deformations damaged roads, rail lines and other lifelines, resulting in major economic disruption. The behavior of the numerous landslides was influenced, in part, by heavy rain associated with Typhoon Tokage. At Nagaoka City, there had been 100 mm (4 inches) on October 20 and 13 mm (.5 inch) on October 21.

The most devastated region in the Unouma Hills, was the village of Yamakoshi that suffered numerous earth slumps. An example of LIDAR imagery is presented for one of these slides located to the east of Yamakoshi. This particular landslide is chosen as it illustrates earthquake-generated slumping seen in many areas proximal to the epicenter. The survey was conducted from two locations on a hillside opposite the slump, and was conducted in steady rain.

Figure 7 is a LIDAR-generated image of the center portion of the slump showing the headscarp, a demolished house, a deformed retaining wall and a small pond formed at the base of the slope due to the damming of the creek. The demolished house was once at the elevation of the blue house hanging at the top of the headscarp. The profile line plots the location of the profile given in Figure 6. The profile indicates that the slump head scarp is approximately 8 meters high, the slump has a total relief is 42 meters and has an average slope is 16.5°. The 3D LIDAR data, once collected can be viewed from any chosen perspective in a 3D computer graphics environment. Figure 7 shows a plan view of earth slump showing the limits as determined by the LIDAR survey as if one were viewing it from the air. Because the data was collected at ground level, many parts of the slide surface were hidden from view and hence could not be sensed by the LIDAR. Survey data of the front faces of buildings show up as lines when projected in a birds-eye view. The geometry of the retaining wall can also be seen. The extent of the slump is measured to be approximately 170 meters wide, 140 meters from head to toe, with a total relief of 42 meter.

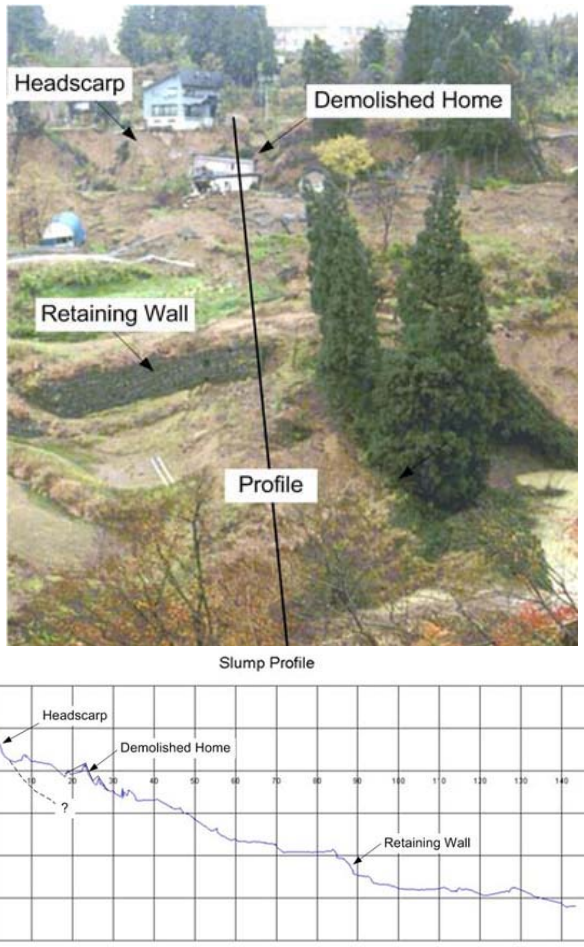

Figure 7. Image acquired by the LIDAR imager system. Profile of slump extracted from the LIDAR data showing a total relief of approximately 42 meters and an average slope of approximately 16.5°.

This map was derived from the LIDAR survey by processing the point cloud data into a digital elevation model using GIS mapping software. The stripes of color represent elevation bands sliced into 1 meter intervals. Note the location of the cross-section and profile that are plotted below. The LIDAR survey was conducted from one strategically positioned tripod setup marked in Figure 9. This plot shows the asymmetry of the side scarp due to the orientation of the rock bedding plane relative to the ground surface. The scarp is approximately 5 meters high on the right (south) flank of the slide and has virtually no relief on the left (north) flank of the slide. The profile line shown in Figure 9 is plotted in Figure 10. This profile shows the planarity of the slide surface that failure along a bedding layer in the downslope direction. Remarkably, the trees found on the lower part of this profile were "rafted" in an upright position down the shear plane riding on a translating block of rock. The rockslide is approximately 70 meters long and 40 meters wide. The uniform slope is 24.6°.

A LIDAR survey of one of two translational rock slides east of Ojiya was completed on November 20, 2004. These two slides were triggered along Highway 291, close to the location where the highway exits the mountains at the Shinano River. Figure 9 is an aerial photograph of the two rockslides. Both occurred along bedding planes on dip slopes dipping about 25° to the west. The LIDAR survey was conducted on the left-most rockslide as shown in Figure 9. The shear surface of this particular rockslide is ideal for Newmark-style analyis as it is remarkably planar and occurred along sandstone bedding planes with a dip-slope orientation. It is this dip-slope geometry along Highway 291 that likely led to the multiple failures in the area and subsequent burial of this section of the highway. Figure 9 also shows a contour map of the rockslide.

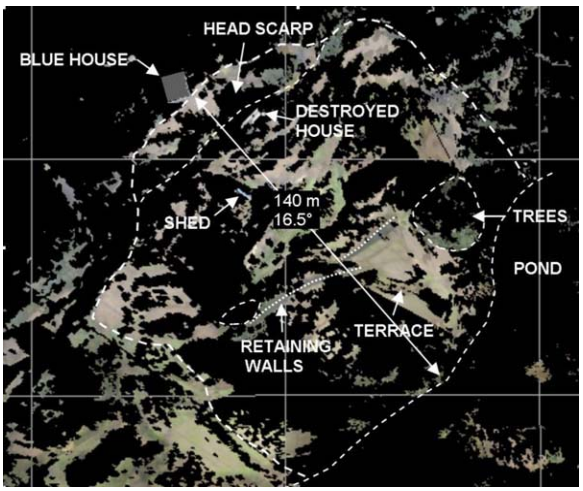

Figure 8. Map view of earth slump showing the approximate limits of major movement as determined by the LIDAR survey

Between the time the aerial photo (Figure 9) was taken and the time of the LIDAR survey, a substantial amount of debris had been excavated from, and adjacent to, the highway. Thus this evidence of slide volume has been lost. This underlines the need for rapid response documentation of earthquake damage before repairs remove critical evidence.

CONCLUSIONS

In this paper, we investigate the applicability of Light Detection and Ranging (LIDAR) to map the settlements at geotechnical earthquake engineering ground failures. There are several benefits in acquiring these LIDAR data after an earthquake. First, the detailed failure morphologies of damaged ground allow researchers to make measurements that were impossible by conventional survey means. LIDAR systems successfully resolve and map complex surface features that are a few centimeters in size. Repeat surveys of georeferenced imagery, for example at the Ishikari site, allow for detailed change detection mapping of surfaces by computing difference maps. A study of the aggregated error

budget of individual scanning, georeferencing, multiscan registration, and surface modeling, finds that the current state of practice allows for position accuracies of several centimenters, at best. At this level of model accuracy, we are able to preserve digital terrain models from LIDAR imagery that will allow for analysis of failure the mechanics of landslides at unprecedented detail.

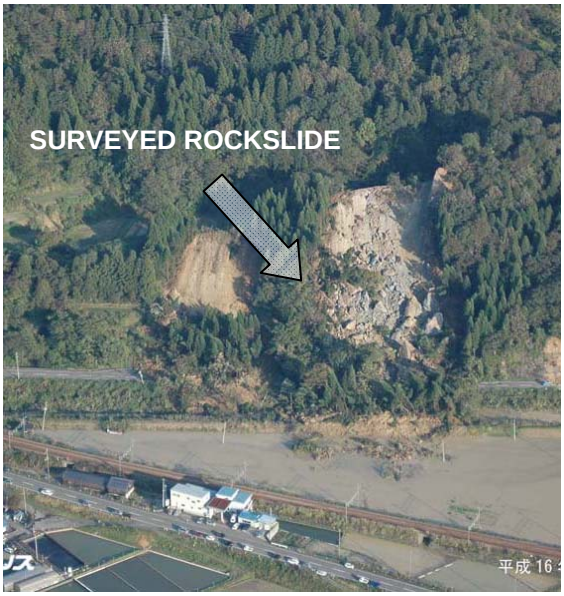

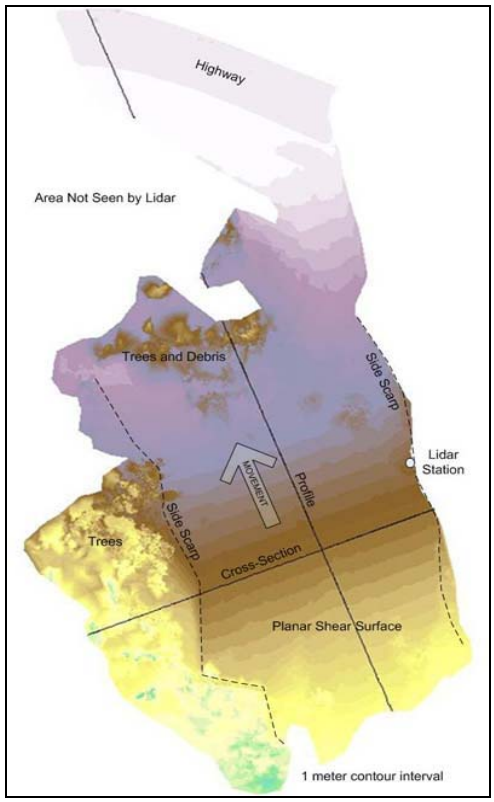

Fig. 9. Aerial photograph of two rockslides in east Ojiya (37.3294N, 138.8259^{E}; courtesy of ORIS. Contour map of the rockslide derived from the LIDAR survey

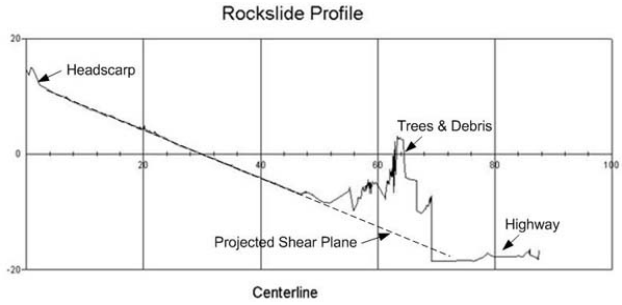

Figure 10. Rockslide cross-section showing the asymmetry of the rockslide depth. The original ground surface is assumed to be a linear projection of the adjacent ground surface.

ACKNOWLEDGMENTS AND APPENDICES

The authors would like to thank Diane Minasian (USGS), Scott Ashford (OSU), Yohsuke Kawamata (OSU) Kobe University, and the Port and Airport Research Institute. The Los Angeles Reservoir study was supported by grants from the Multidisciplinary Center for Earthquake Engineering Research and a Master Agreement No EEC-970147 from the National Science Foundation. The City of Los Angeles Department of Water and Power funded the surveying and airborne LIDAR work. The Niigata work was made possible by funding through the Earthquake Engineering Research Institute (EERI) and the Geo-Engineering Earthquake Reconnaissance (GEER) activities of the U.S. National Science Foundation (Grants CM MI-0323914 & CMMI-0131895), and cost sharing by the U.S. Geological Survey. The Ishikari study was supported by National Science Foundation award number CMMI-0728120.

REFERENCES

I-SiTE Inc. (2007). "3D Laser Scanning Software", 1 December 2007. http://www.isite3d.com

Kayen, R.E., Pack, R. T., Bay, J., Sugimoto, S., and Tanaka, H. (2006). "Terrestrial-LIDAR visualization of surface and structural deformations of the 2004 Niigata Ken Chuetsu, Japan, earthquake," Earthquake Spectra, 22, S147-162.

Kayen, R. E.; Stewart, J. P.; Lembo, A. J.; Hu, J.; Davis, C. A.; Hogue, T.; Collins, B. D.; Minasian, D.; Louis-Kayen, N. M.; O'Rourke, T. D. (2008) Comparison of Coincident Terrestrial and Airborne LIDAR Datasets with Respect to Detection of Ground Metrics and Topographic Change, American Geophysical Union, Fall Meeting 2008, abstract #G52A-08

Kayen, R. E.; Stewart, J. P.; Lembo, A. J.; Hu, J.; Davis, C. A.; Hogue, T.; Collins, B. D.; Minasian, D.; Louis-Kayen, N. M.; O'Rourke, T. D. (2009) Terrestrial and Airborne LIDAR: Comparison of Coincident Datasets for Measuring Ground Deformation and Topographic Change, Eos Trans. AGU, 90(22), Jt. Assem. Suppl., Abstract G31A-02

Minasian, D.; Kayen, R.; Ashford, S.; Kawamata, Y.; Sugano, T., "Ground Deformation Analysis of Blast-Induced Liquefaction at a Simulated Airport Infrastructure Using High Resolution 3D Laser Scanning," American Geophysical Union, Fall Meeting 2008, abstract #G52A-01, 2008.

Riegl (2007). "Terrestrial scanning laser systems," 1 December 2007. http://www.rieglusa.com

Stewart, J.P., Hu, J., Kayen, R.E., Lembo, A.J. Jr., Collins, B.D., Davis, C.A., and O'Rourke, T.D. (2009). "Use of airborne and terrestrial LIDAR to detect ground displacement hazards to water systems," Journal of Surveying Engineering, ASCE, 135 (3), 113-124.